MR Elastography Using the Gravitational Transducer

Omar Isam Darwish[1,2]; Vitali Koch[3]; Thomas Joseph Vogl[3]; Marcos Wolf[4]; Katharina Schregel[5]; Arnie Purushotham[6]; Valerie Paradis[7,9]; Valerie Vilgrain[8,9]; Radhouene Neji[1]; Ralph Sinkus[1,10]

[1]School of Biomedical Engineering and Imaging Sciences, King's College London, United Kingdom
[2]MR Predevelopment, Siemens Healthineers, Erlangen, Germany
[3]Department of Diagnostic and Interventional Radiology, University Hospital Frankfurt, Frankfurt am Main, Germany
[4]Centre for Medical Physics and Biomedical Engineering, Medical University of Vienna, Austria
[5]Department of Neuroradiology, Heidelberg University Hospital, Heidelberg, Germany
[6]School of Cancer & Pharmaceutical Sciences, King's College London, United Kingdom
[7]Department of Pathology, Hôpital Beaujon, Clichy, France
[8]Department of Radiology, Hôpital Beaujon, Clichy, France
[9]Université Paris Cité, INSERM, Centre de recherche sur l'inflammation, Paris, France
[10]Laboratory for Vascular Translational Science (LVTS), INSERM U1148, Paris, France

Introduction

Biomechanical integrity is at the heart of the body's homeostasis. Many pathologies manifest themselves by impacting tissue stiffness. These include chronic liver diseases, which cause inflammatory and fibrotic processes that lead to a "stiff liver". For a long time, liver palpation was used to estimate liver size, feel for liver stiffness, and possibly local masses to find signs of liver disease. However, the development of ultrasound elastography (USE) [1] and MR elastography (MRE) [2, 3] changed this radically by providing quantitative maps of tissue stiffness, and even tissue viscosity when done in 3D [4]. MRE has demonstrated its ability to non-invasively assess chronic liver disease [5, 6] and characterize breast cancer lesions [4, 7] and brain tumors [8, 9]. Currently, hepatic MRE is the most applied elastography technique in the clinic, where it is used to quantify liver fibrosis by measuring the shear stiffness [10] or the shear wave speed [6]. In addition, it has shown promise in grading liver inflammation by measuring the loss modulus [6].

In general, elastography utilizes the intricate link between the properties of propagating mechanical shear waves, i.e., their amplitude, phase, and local wavelength, to uncover the underlying mechanical properties of tissue. Importantly, soft tissue is quasi-incompressible since it consists of 70% water, sometimes even more. Thus, the typical physician's notion of tissue being "more or less compressible" is based on the wrong terminology: Tissue can be sheared to a certain extent given an exerted force, but it does not change its volume as water is incompressible. The spatially varying constitutive material properties result

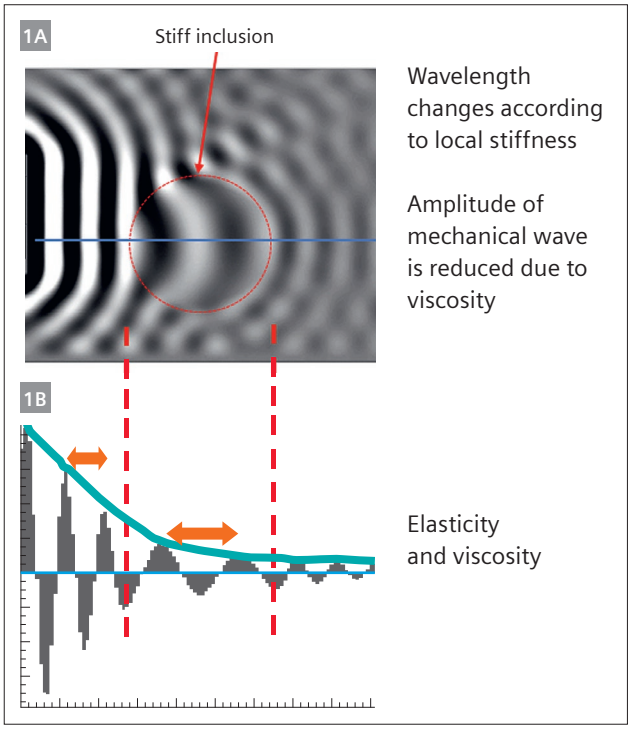

1 **Dependence of shear wavelength on local stiffness**
(1A) Finite element simulation of a wavefield with a homogeneous background and a hard inclusion. **(1B)** The corresponding line profile shows that the local wavelength (orange arrows) changes depending on the underlying stiffness. Additionally, the amplitude of the wave drops due to intrinsic loss mechanism (viscosity). "Imaging" the shear wave allows hence in return to recover the local biomechanical properties.

in shear waves propagating faster or slower depending on whether tissue is locally stiff or soft, respectively (Fig. 1). For a fixed vibrational frequency, this translates into a longer or shorter wavelength, which can be imaged via phase contrast-based MRI sequences [3, 4, 11, 12].

Overall, MRE necessitates three essential steps:

I) Efficient wave generation and penetration in a patient-friendly way
II) Wave image acquisition using phase-locked and motion-sensitized MRI sequences that yield high spatial fidelity
III) Recovery of the underlying biomechanics in the most unbiased fashion

Shear wave generation: MR Elastography transducer

The generation of monofrequent shear waves with sufficient amplitude and phase stability within the MRI environment is a non-trivial task. To date, several MRE transducer concepts have been proposed [19] with very different driving approaches:

I) Current-driven electromagnetic coils that oscillate due to the Lorentz force in the main B_0-field [4, 13, 20]
II) A pneumatic approach connecting an active driver with a membrane via a flexible tube [21]
III) A pulse-density modulated approach using compressed air [22]
IV) A gravitational transducer approach [23]

For MRE to yield high-quality maps of biomechanical properties, the transducer needs to transmit a pure frequency spectrum. Otherwise, parasite frequencies (upper harmonics) impact in particular the quality of the viscous biomechanical properties [24]. Each transducer concept has pros and cons, which relate to flexibility, strength, pureness of the frequency spectrum, and the ability to transmit waves even under the application of external mechanical load, e.g., when the transducer is positioned at the back of the patient. Here we focus on the description of the gravitational transducer approach and discuss its properties.

A gravitational transducer utilizes the generic equivalence of acceleration to force with a rotating eccentric mass for the generation of vibrations, similar

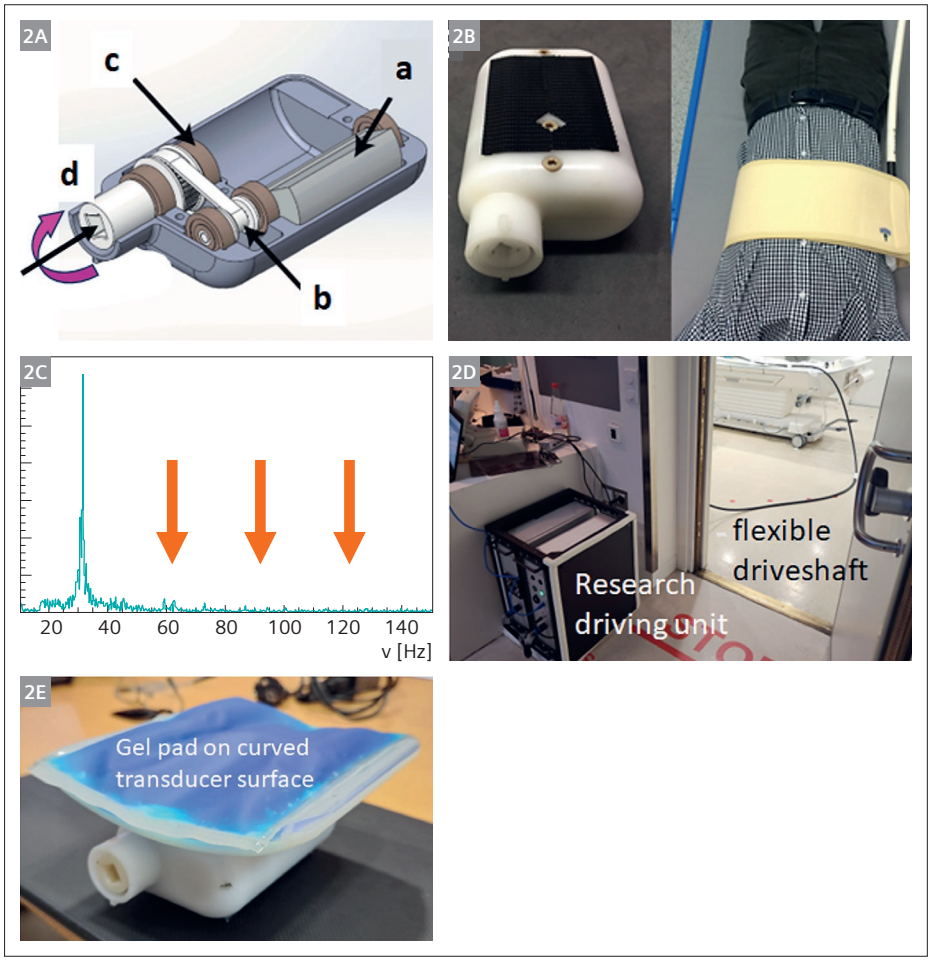

2 Gravitational transducer concept **(2A)** The gravitational transducer consists of a casing that hosts a spinning eccentric mass (a), which is connected via a gearbox (b, c) to an external flexible driveshaft (d). **(2B)** The closed transducer is very compact and, for abdominal applications, is strapped to the patient's body via a belt. **(2C)** When operated at 30 Hz, the frequency response spectrum shows no upper harmonics. **(2D)** The research prototype of the gravitational MRE concept had the driving unit outside the MRI room, with the flexible driveshaft going through the waveguide toward the patient table. The picture shows the installation at University Hospital Frankfurt am Main, Germany. **(2E)** To improve patient comfort for abdominal applications, the transducer has a curved contact plate with a gel pad. The curvature and size of the contact plate are easily adaptable to different applications.

to those found in a mobile phone's vibrating alert motor. Figure 2A shows a sketch of the transducer design: The eccentric mass (a) is connected via a gearbox (b, c) to an external flexible driveshaft (d). The presence of the gearbox allows to reduce the friction on the external driveshaft. A rotating eccentric mass has the advantage that the generated force grows with increasing frequency quadratically, which leads to a vibrational amplitude independent of frequency [23]. This is in stark contrast to acoustically driven (pneumatic) approaches, which always experience a reduction in amplitude with increasing frequency. The compact design of the transducer enables various abdominal or cerebral applications (Fig. 2B) as the mass rotates independently of whether any external load is applied to the casing of the transducer.

Typically, the loss in amplitude for acoustically driven approaches is compensated by an increase in driving power, which leads in turn to a non-linear system response, i.e., the presence of upper harmonics. This leads to a degradation of data quality. The gravitational approach – by contrast – represents a linear system with a frequency response spectrum devoid of any upper harmonics (Fig. 2C). This concept, which was developed within an EU-funded Horizon 2020 project (FORCE) at St Thomas' Hospital (part of King's College London), had the driving unit outside the MRI scanning room with the flexible driveshaft reaching through the waveguide and finally connecting to the transducer at the patient bed (Fig. 2D). To ensure patient comfort, the transducer has a curved contact plate cushioned with a gel pad. The gel pad allows compressional waves to pass without any attenuation into the patient's body, while shear vibrations of the transducer are dampened, which increases patient comfort. This flexible design allows for easy adaption to other organs such as kidney, breast, and brain.

MR Elastography sequence

MRE and diffusion-weighted imaging (DWI) sequences share many properties: They both are intended to quantify motion of moving water molecules using motion-sensitized sequences. The fundamental difference between the concepts is that in diffusion we do not know when the individual water molecules are jumping in time due to the Brownian motion. Hence, DWI is based on the concept of signal destruction without any impact on the net phase of the MR image [25]. In MRE, however, time is controlled via the vibration of the mechanical transducer. Hence, it is possible to use a phase-locked approach to visualize the micron-level vibrations within the phase of the MR image [4, 13]. Many phase-contrast MRI sequences can be used for MRE; however, gradient-echo (GRE) and spin-echo echo-planar imaging (SE-EPI) sequences are the ones most frequently employed. The fundamental concept of the phase-locking is shown in Figure 3. The frequency of the motion-encoding gradient (MEG) should be identical with the mechanical vibration frequency to obtain the largest sensitivity to motion. At 60 Hz, this leads to very long echo times (TE), which requires the utilization of SE sequences to recover sufficient signal-to-noise ratio (SNR), especially when operating at 3T. Consequently, a single SE-based excitation-readout block spawns over approximately 50–66 ms (Fig. 3B). Temporal delays (orange blocks in Fig. 3B) allow to shift the MR acquisition relative to the mechanical vibration, providing images of the wave propagation at another timepoint (wave phase) throughout the oscillatory period of one mechanical vibration. Typically, 4 to 8 of such wave phases equally spaced over one oscillatory cycle are acquired to recover later – during the MRE reconstruction process – the complex-valued displacement field. The long TE results in prohibitively long acquisition times, which can be counterbalanced via EPI readout approaches. Depending on echo spacing, phase field of view (FOV), and off-resonance, EPI leads to geometrical distortions, which in turn will impact the recovery of the biomechanical properties, because higher-order spatial derivatives of the wavefields are necessary for solving the wave equation. GRE-based sequences using MEGs at the mechanical vibration frequency are one way to shorten acquisition time [26]. However, the long TE of ~20 ms results in very poor SNR. The use of fractional MEGs overcomes this limitation by sacrificing sensitivity to motion by shortening the MEG, which therefore no longer operates at the mechanical vibrational frequency [11]. The corresponding loss in phase-to-noise ratio for wave propagation imaging can be partially recovered by more advanced motion-encoding concepts such as Hadamard encoding [27]. Initial approaches used excitation readout blocks with durations that were still integer multiples of one mechanical oscillation period (Fig. 3C) [28]. More advanced approaches incorporated the temporal delays into the duration of each individual shot, leading to a further shortening of the scan time (Fig. 3D) [12]. Now, simultaneous multi-slice (SMS) excitation [29] has opened the gateway to shortening acquisition time even more, by enabling the capture of 3D datasets within one single breath-hold (Fig. 3E) [30]. Spiral readout concepts have also been proposed for brain MRE [31], including self-navigation for motion correction. Here again, due to the long readout, B_0 inhomogeneities and eddy-current effects need to be properly compensated to avoid any impact on the fidelity of space.

MR Elastography reconstruction

The MRE sequence provides snapshots of the wavefield at different timepoints (wave phases) throughout an oscillatory cycle (Fig. 4). Thus, when presented as a function of

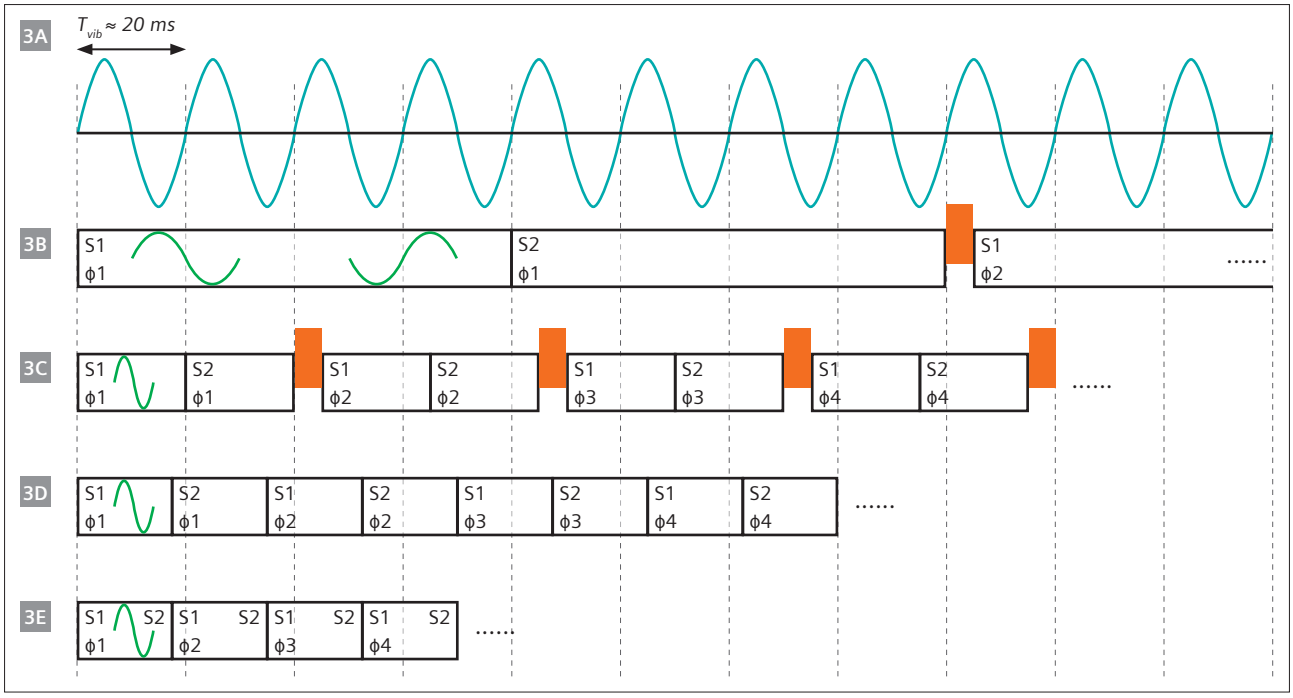

3 **MRE sequence concepts**
(3A) Sinusoidal mechanical vibration generated by the MRE transducer is for clinical applications typically in the 40–60 Hz range. Thus, one period corresponds to roughly T_{vib}~20 ms. **(3B)** SE-based sequences typically use MEGs (green) that operate at the vibration frequency. This leads to a long shot duration, i.e., the time interval encompassing excitation and readout. Temporal delays (orange rectangles) are used to shift to the next wave phase ϕ_j (j∈[1,2,3...M], M = number of wave phases) once all slices S_i have been acquired (i∈[1,2,3...N], N = # of slices). **(3C)** Fractional motion-encoding concepts enable significant scan-time reduction at the cost of a loss of motion sensitivity. Initial approaches still had the temporal delays separate from each shot, thereby perturbing the eddy-current steady state [12]. **(3D)** More sophisticated concepts overcame this by incorporating the delays into each shot, further reducing scan time. **(3E)** SMS finally provided a straightforward way to acquire 3D MRE datasets within a single breath-hold.

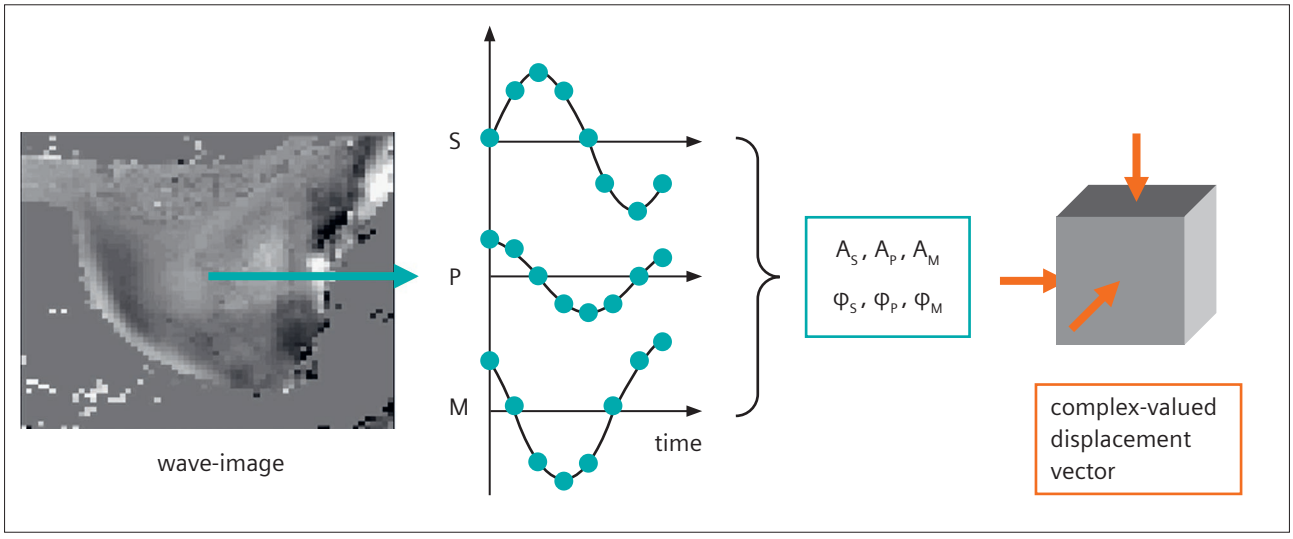

4 **From MRE raw data to wavefield displacement vector**
The MRE data acquisition provides snapshots of the propagating wave. When looked at pixel-wise, a sinusoidal modulation of the MRI phase is observed for each of the three encoding directions (readout [M], phase-encoding [P], slice direction [S]). A temporal Fourier transform yields the corresponding amplitudes A_i and phases φ_i of the complex-valued displacement vector of the wavefield in direction $i \in$ (M, P, S). This approach assumes temporal steady state, i.e., there are no transient effects, and the time component is purely described by sinusoidal temporal modulation at the driving frequency.

wave phase, each encoding direction will show for each single pixel a sinusoidal temporal MRI-phase modulation. A temporal Fourier transform then yields the corresponding amplitudes A_i and phases φ_i of the wavefield, which constitute the steady-state solution to the problem.

The wave propagation is in general a 3D problem and can only, under specific boundary conditions, be simplified to 2D or even 1D [1]. The beauty of the MRE approach is that the measured displacement field constitutes the underlying wave solution of the problem at hand. Certainly,

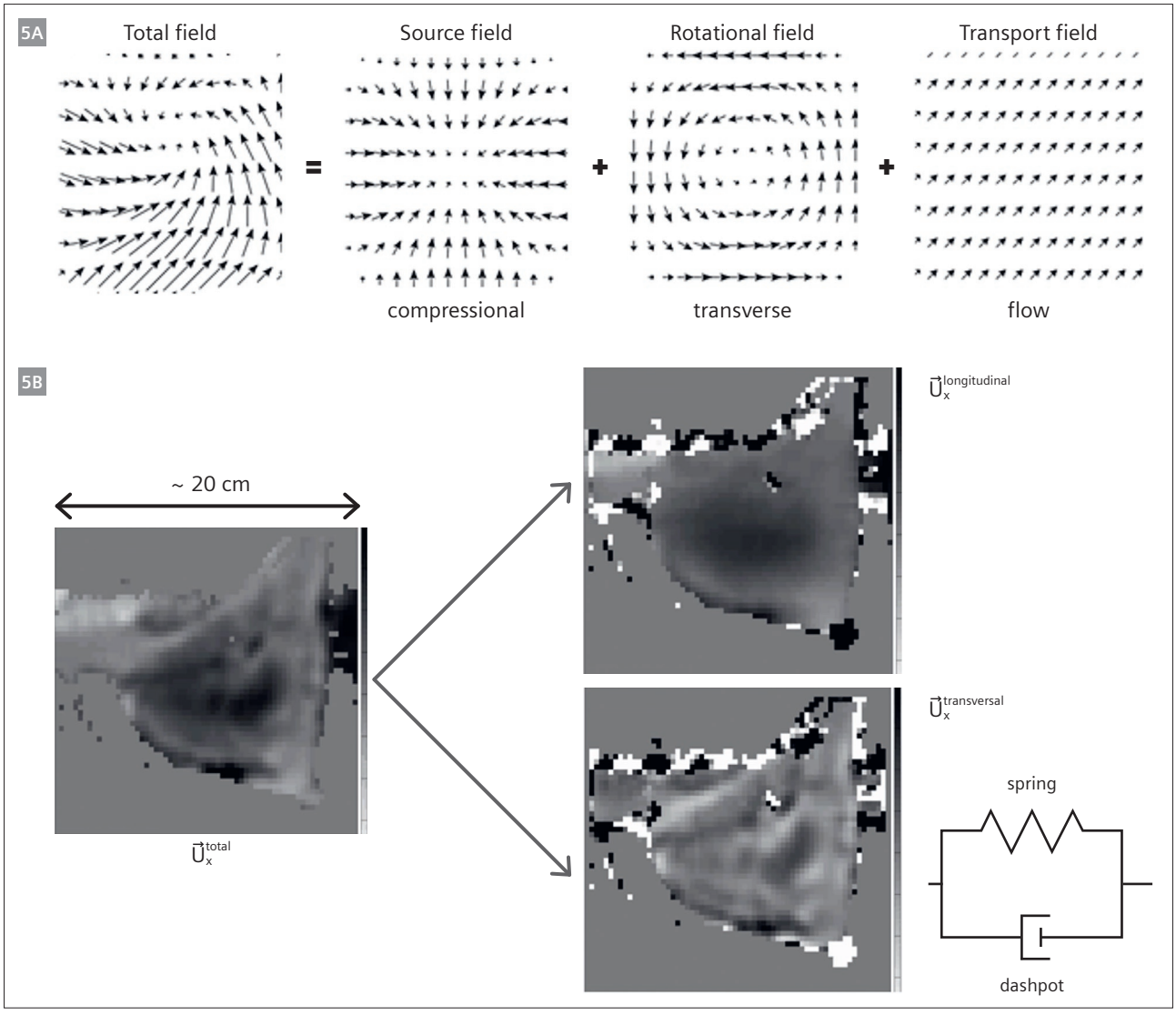

5 Mathematical foundations of MRE reconstruction

(5A) In general, any wavefield is the sum of three fields that exhibit very different mathematical properties: a source field, a rotational field, and a transport field. In our case, the total displacement vector is the sum of the compressional (source) and the transverse (rotational, shear) wave, because there are no transport effects in our experiments. **(5B)** Both waves exhibit very different mathematical properties and different wavelengths since they are coupled to different mechanical properties of tissue, shown here for in vivo data in breast tissue. The compressional wave in our frequency domain has a very long wavelength (~cm) as it is linked to the bulk modulus. Remember that tissue is incompressible, leading to a bulk modulus in the order of GPa. Conversely, the shear wave is relatively short (~cm) as it is linked to the shear modulus (~kPa). Note that both moduli differ by six orders of magnitude! The solution of the complex-valued shear modulus can now be interpreted in many ways: One possibility is to view tissue as if shear stiffness (elasticity, spring) and shear loss (viscosity, dashpot) were organized as spring and dashpot connected in a parallel fashion (Voigt model). In reality, tissue exhibits a more complex mechanical response function, leading to fractal-like mathematical representations due to its hierarchical organization.

boundary conditions do impact the details of the wavefield due to reflections and scattering. Since the underlying physics is local, except under specific quantum mechanical conditions [32], all we need to do is invert the 3D wave propagation equation [33]. Mathematically, any continuous vector field can be decomposed into three different components which carry very different mathematical properties:

I) One field that has sources (curl-free)
II) One field that – similar to the magnetic field – has no start and no end (divergence-free)
III) One field that relates to transport effects (curl- and divergence-free, Fig. 5A) [34]

In our case, due to the absence of any transport effects (there is no flow of tissue present in the data), the total displacement field is the sum of the compressional and the transverse (shear) wavefield (Fig. 5B). These two fields probe very different properties of tissue: The compressional wavefield is linked to the bulk modulus of tissue and propagates at the speed of sound in water, i.e., at 1550 m/s. Hence, it exhibits very long wavelengths, which are around ~30 m at frequencies of around 50 Hz. This is mathematically very challenging to handle, given the typical SNR in MRE data. The transverse wave, by contrast, travels at speeds of around 1–10 m/s resulting in wavelength of around 2–20 cm! Given typical pixel-sizes of ~3–4 mm, such wavelengths can properly be resolved and used to calculate spatial derivatives of a higher order. For a correct inversion of the wave equation, it is necessary to first remove the compressional field. Using, for instance, its mathematical properties of "carrying" the sources of the mechanical wavefield, it is possible to mathematically remove it via the "curl operator". Certainly, this is at the cost of an additional spatial derivative [17]. Other approaches try to remove the compressional component via high-pass filters in the Fourier domain [18], or via integration [35]. A combination of both utilizes divergence-free basis functions in the context of finite element modelling [24]. Once the compressional field has been removed, the remaining equation is basically expressing Hooke's law: Stress and strain are related via the shear modulus [33]. The beauty in MRE is that the approach to solve for the complex-shear modulus is independent of any assumptions of the underlying rheological properties of tissue [17, 36]. The single most important assumption is that the material is isotropic and linear. Thus, shear modulus (elasticity) and loss modulus (viscosity) of the complex-valued shear modulus can be interpreted a posteriori in terms of the Voigt model, which assumes tissue to behave as a spring and a dashpot in parallel (Fig. 5B). In reality, tissue exhibits far more complex dispersion (i.e., frequency-dependent) properties, which are likely to carry valuable diagnostic information [37, 38].

It is important to stress that both elasticity and viscosity relate to the solid shear properties of the material, and the loss describes the ability of the material to extract energy from the propagating wave. The origin of this energy loss can be true absorption (i.e., conversion to heat) or scattering (leading to a redistribution of the wave's energy in space). Scattering-induced effects within tissue impact the frequency dependence of tissue and lead to an intricate mixture of constitutive and apparent effects governing the dispersion properties [39].

Figure 5 shows the overarching mathematics and physics governing the 3D wave propagation. Under certain assumptions, however, it is possible to simplify the 3D equation, which after all necessitates the measurement of the 3D displacement vector within a volume and the calculus of third-order spatial derivatives, which puts high demands on the SNR of the data. Another approach assumes that the total wavefield is composed of independent plane waves, and cuts out in Fourier space a "pie-chart" section to virtually recover the individual plane waves (Figs. 6A–6C) [18]. Additionally, low-pass and high-pass filters are utilized to suppress noise and compressional wave components, respectively. The resulting wave is a quasi-plane-shear-wave, which allows to recover local stiffness values without needing to measure all wave components within a volume (Figs. 6D, 6E). Clearly, this method relies on several assumptions which are not always met. It is nonetheless a rather robust technique which enables quantification of liver stiffness within a single breath-hold [40]. However, recovery of tissue viscosity requires the full solution of the 3D wave equation since the previous mathematical operations impact too strongly on the imaginary part of the wave equation to obtain reliable values (Fig. 6F).

MR Elastography examples using the gravitational transducer Ultrasound gel phantom

Quality control in MRE is essential to ensure correct performance of the intricate interplay between MRI data acquisition and mechanical vibration. Figure 7A shows results from an ultrasound (US)-based phantom (Ultragel 2000 Hungary, GUS5LT) that exhibits at 60 Hz a shear modulus of ~0.9 kPa and has few dispersive properties. The semi-rigid plastic-based surface of the phantom leads to a grid-like pattern of shear waves

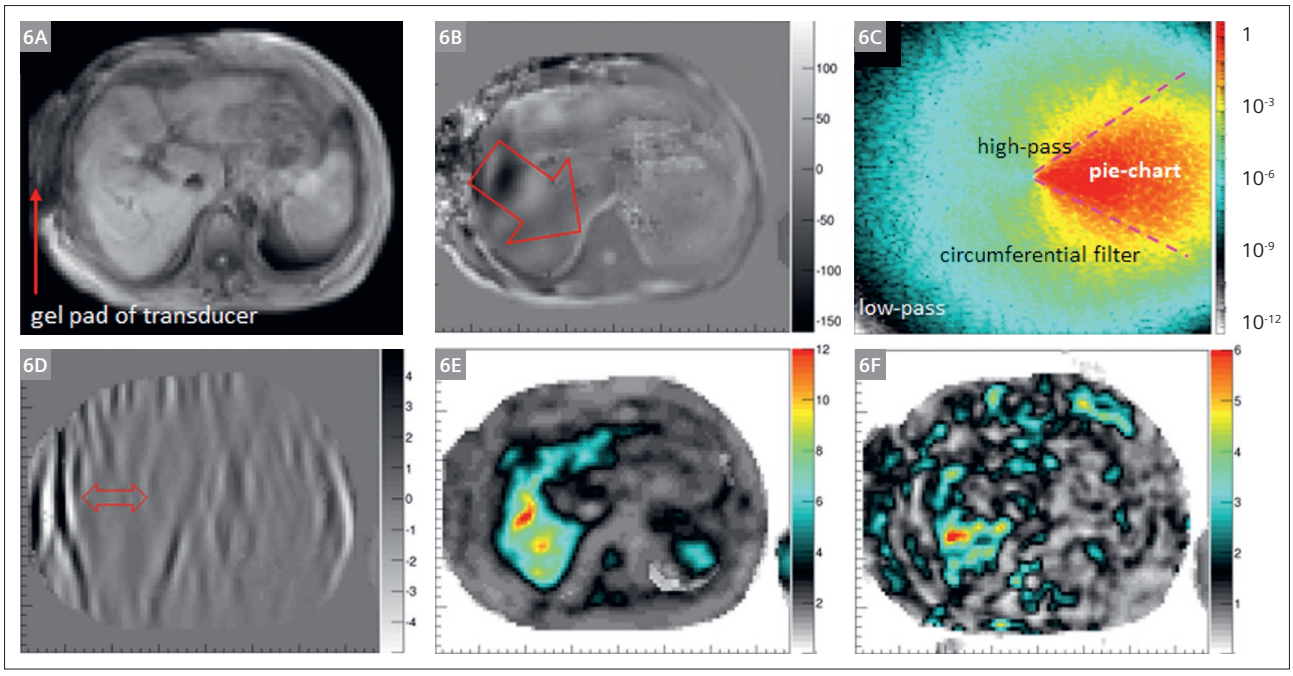

6 **Directional wave filtering for 2D MRE and viscosity**
(6A) Magnitude image of the liver in transverse orientation. The gravitational liver transducer is located on the right-hand side of the patient with the gel pad visible (arrow). **(6B)** The pattern of the wavefield in through-slice direction shows mainly a plane wave propagating toward the center of the patient (arrow, [mm]). **(6C)** Amplitude of the Fourier transform of the wave image shown in 6B segmented in a pie-chart fashion with additional low-pass, high-pass, and circumferential filters to generate a virtual plane shear wave in image space after inverse Fourier transform. Note that the Z-scale is logarithmic. **(6D)** Corresponding plane-shear wave image showing longer wavelengths within the liver when compared to regions of subcutaneous fat (arrow). **(6E)** Result of the 2D approximation depicting an elevated shear stiffness of the liver in a patient with severe liver fibrosis (grade F4) [kPa]. **(6F)** Corresponding map of the shear viscosity resulting from a full 3D inversion of the wavefield [kPa]. Data from University Hospital Frankfurt am Main, Germany.

within the US gel (Fig. 7B). The directional filter is capable of extracting the individual plane waves, with Figure 7C showing one of the waves travelling from left to right (arrow). The corresponding 2D inversion yields a stiffness of

$$|G^*| = 0.9 \pm 0.1 \text{ kPa}$$

which is confirmed by the 3D inversion (Figs. 7D, 7E). The 3D inversion additionally allows quantification of the shear viscosity (G_l), which is very low for such a gel, naturally. A very homogeneous phase angle of

$$Y = 0.1 = \frac{2}{\pi} \operatorname{atan}\left(\frac{G_l}{G_d}\right)$$

is retrieved, and is indicative of a material that is mostly spring-like with few absorptive properties.

Liver

The mechanical integrity of the liver can be affected by a broad spectrum of diseases, including viruses, drugs, alcohol, or the metabolic syndrome. Metabolic dysfunction-associated steatotic liver disease (MASLD), formerly called non-alcoholic fatty liver disease (NAFLD), is the most common chronic liver disease in Western populations and is continuously increasing in prevalence due to lifestyle changes, obesity, and type 2 diabetes mellitus [41]. Metabolic dysfunction-associated steatohepatitis (MASH), formerly called non-alcoholic steatohepatitis (NASH), is generally considered the advanced type of MASLD. It is characterized by hepatic inflammation, hepatocellular injury, and fibrogenesis [41]. Lipotoxicity with ongoing inflammation is considered the major pathogenic driver of MASH, aggravating liver injury and promoting liver fibrosis [42]. In approximately 20% of cases, MASH

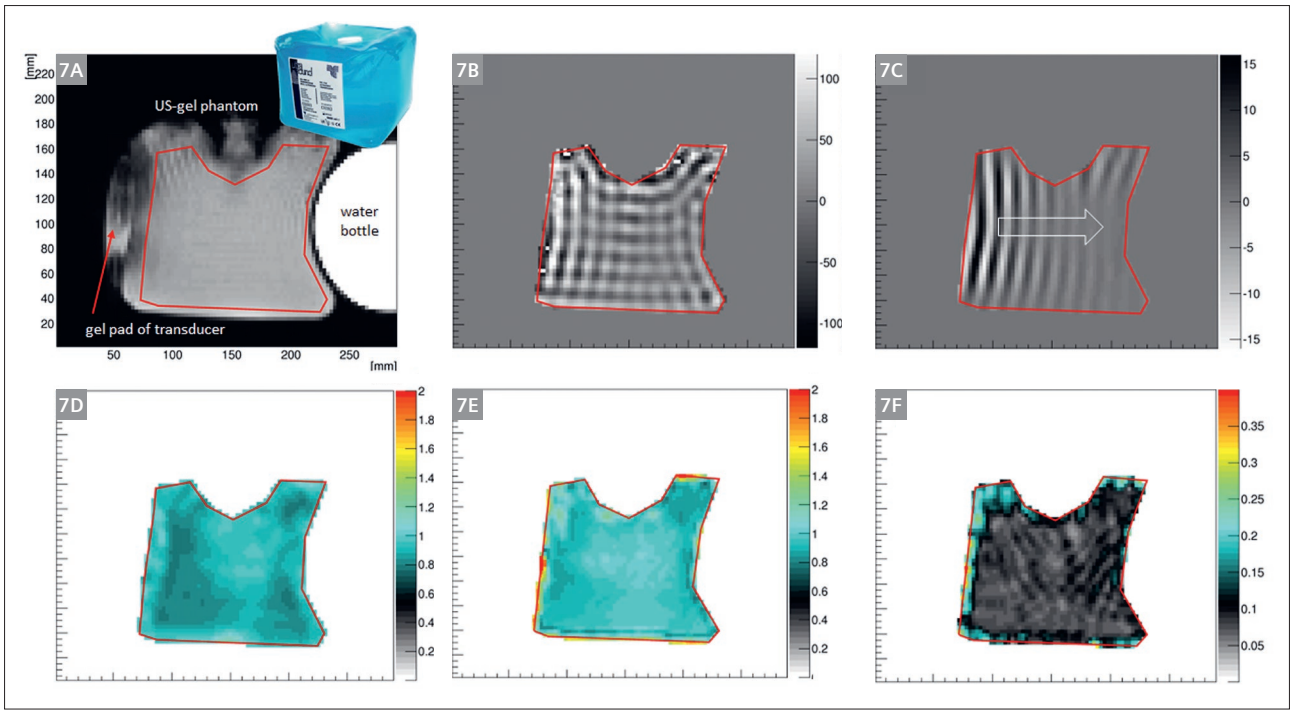

7 Ultrasound gel phantom results

(7A) Magnitude image of the experimental setup. A water bottle is attached to the US phantom to increase its weight. **(7B)** The real part of the displacement field in through-slice direction showing a grid-like pattern, which originates from the boundary conditions of the phantom, i.e., its semi-flexible plastic surface. **(7C)** One of the plane waves that was extracted from the directional filter approach here is travelling from left to right in the image. **(7D)** Magnitude of the complex shear modulus recovered from the 2D approach. The mean value agrees very well with the corresponding gauge obtained via the 3D inversion **(7E)**. **(7F)** Phase angle Y∈[0,1] of the phantom as obtained from the 3D inversion indicating that the material is exhibiting mainly spring-like properties.

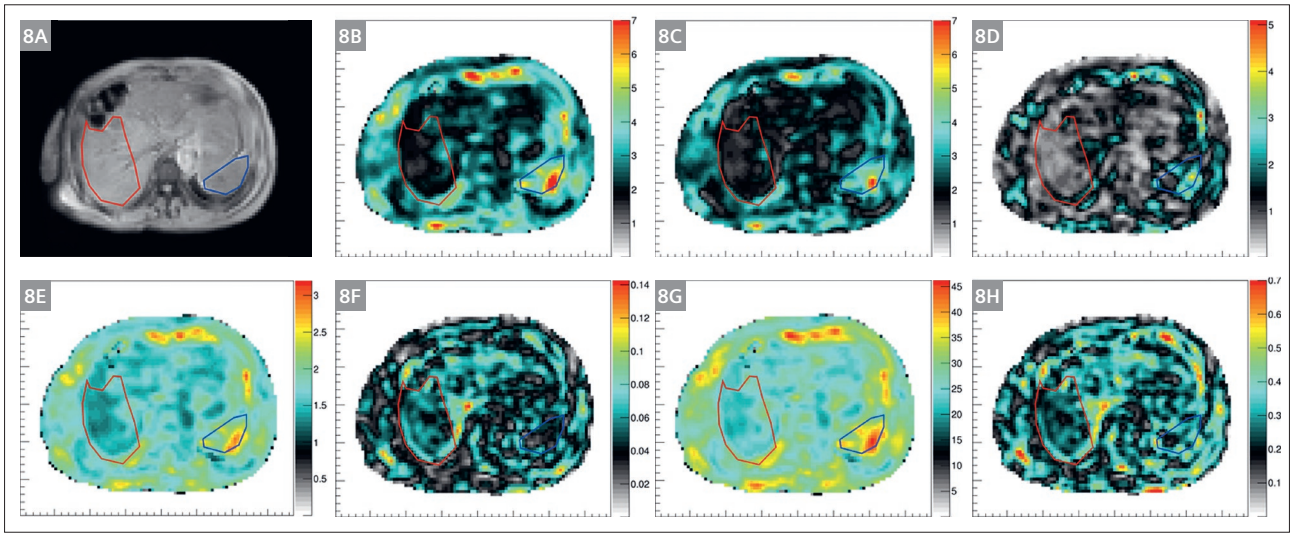

8 3D MRE results in the liver

(8A) Magnitude image of a liver patient with low-grade fibrosis related to metabolic dysfunction-associated steatohepatitis (MASH). **(8B)** Magnitude image of the complex shear modulus $|G^*|$ [kPa]. **(8C)** Shear elasticity Gd [kPa] **(8D)** Shear viscosity Gl [kPa]. **(8E)** Shear speed Cs [m/s]. **(8F)** Shear absorption a [1/mm]. **(8G)** Shear wavelength λ [mm]. **(8H)** Shear phase angle Y [0-1]. Data from University Hospital Frankfurt am Main, Germany.

progresses to cirrhosis with increased overall mortality and sometimes the need for liver transplantation [43]. Early identification and initiation of targeted therapy are important to improve patient prognosis. Given the invasive nature of liver biopsy, which carries the risk of numerous complications, MRE emerges as a precise and non-invasive method for evaluating viscoelastic tissue characteristics at first presentation and during follow-up. Due to its ability to evaluate a substantial portion of the liver, MRE can detect focal viscoelastic disparities in all liver segments, in contrast to liver biopsy or transient elastography. Figure 8 shows an example of gravitational 3D wave-encoded MRE applied to a patient with low-grade fibrosis related to MASH. The liver (red region of interest, ROI, in Figure 8B) appears soft with an average value of the magnitude of the complex shear modulus

$$|G^*| = \sqrt{Gd^2+Gl^2}$$

of around 2 kPa. Conversely, the spleen (blue ROI in Figure 8B) shows values of around 4.5 kPa, indicating considerably higher stiffness. This difference is similarly reflected in the elasticity Gd (Fig. 8C) as well as in the viscosity (Fig. 8D). While both elasticity and viscosity express the biomechanics from the point of view of the material, it is equally possible to express it from the point of view of the propagating wave. Numbers can thereby be matched to ultrasound elastography when properly considering dispersive effects, since US-based concepts using acoustic radiation force to generate shear waves are operating at a higher central excitation frequency (~150 Hz). Figure 8E shows the corresponding image of the shear wave speed with the wave propagating faster in the spleen than in the liver. Intriguingly, the wave absorption is higher in the liver than in the spleen (Fig. 8F). The most simple and robust quantity which can be extracted from the wave equation is the shear wavelength (Fig. 8G). As expected, the shear wavelength is short in this patient's liver, while larger in the spleen, reflecting the corresponding soft and stiff material properties (Fig. 1). The last biomarker which carries great potential in quantifying subtle changes in tissue mechanics is the shear phase angle Y, which reports the ratio of shear viscosity to shear elasticity scaled to the range [0–1]. A value close to zero indicates a mainly elastic behavior (spring-like) of the material, while a value close to one is indicative of viscous dashpot-like behavior. Clearly, the spleen is exhibiting a higher phase angle, which shows that its overall behavior is more dashpot-like than that of the liver. Current research is focusing on exploring which biomarker carries which diagnostic value. We have so far seen a linear behavior of shear speed with liver fibrosis grade, and a non-linear relationship between viscosity and inflammation [6, 30]. Intriguingly, the phase angle Y has shown very little to no dependence on the underlying pathology.

Kidney and prostate

Figures 9A and 9B depict an example of 3D wave-encoded MRE applied to the kidney. The gravitational transducer is located on the posterior-lateral abdominal wall of the patient and is emitting waves in AP direction. Cortex, medulla, and central liquid zone are all well distinguishable in the corresponding maps of the shear speed. Note that liquid is extremely soft in terms of shear, while very stiff regarding compression due to its incompressible nature. Also, shear wave speed is well aligned with the anatomical image, as the renal sinus is reaching into the cranial part of the kidney. Figures 9C and 9D show an example of the application to the prostate with the transducer strapped

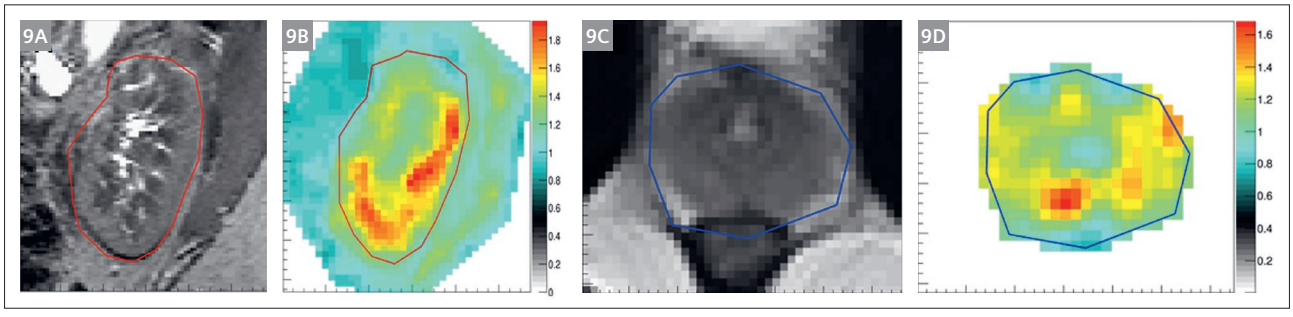

9 **3D wave-encoded MRE results in the kidney and the prostate**
(9A, 9B) T2-weighted anatomical image of the kidney and corresponding image of the shear wave speed [m/s]. Data from University Hospital Vienna, Austria.
(9C, 9D) T2-weighted anatomical image of the prostate and corresponding image of the shear speed [m/s]. Data from University Hospital Frankfurt am Main, Germany.

against the pubic bone and the patient in supine position. The urethra as well as the different zones within the prostate are well delineated in the speed map.

Breast

The application of MRE to the breast [48] necessitates adaptation of the gravitation transducer to the anatomical constraints of the breast coil [49, 50]. This was done in the context of the EU-funded Horizon 2020 project (FORCE at King's College London), in which the transducer was incorporated into the breast MRI biopsy coil. Figure 10 shows results from a breast cancer patient, where the presence of the tumor is well depicted within the shear wave speed image. The corresponding Z-component of the curl field shows that wave propagation is complex, similar to the case of brain MRE (Fig. 11), hence the plane-wave assumption for performing 2D reconstruction approaches might be challenged. MRE is currently under investigation in women undergoing neoadjuvant chemotherapy for breast cancer to determine response or resistance of the tumor early during treatment. Should MRE prove to be a useful biomarker of response or resistance, it will enable oncologists to switch patients who are not responding to a particular drug regimen of neoadjuvant chemotherapy to an alternative drug regimen or guide the patient to early surgical intervention. This can minimize unnecessary toxicity due to an ineffective chemotherapeutic regimen and thereby improve quality of life.

Brain

The application of MRE to the human brain is challenging due to the protective nature of the skull. The transducer is located within the head coil, transmitting waves in an inclined fashion to generate wave motion in all three

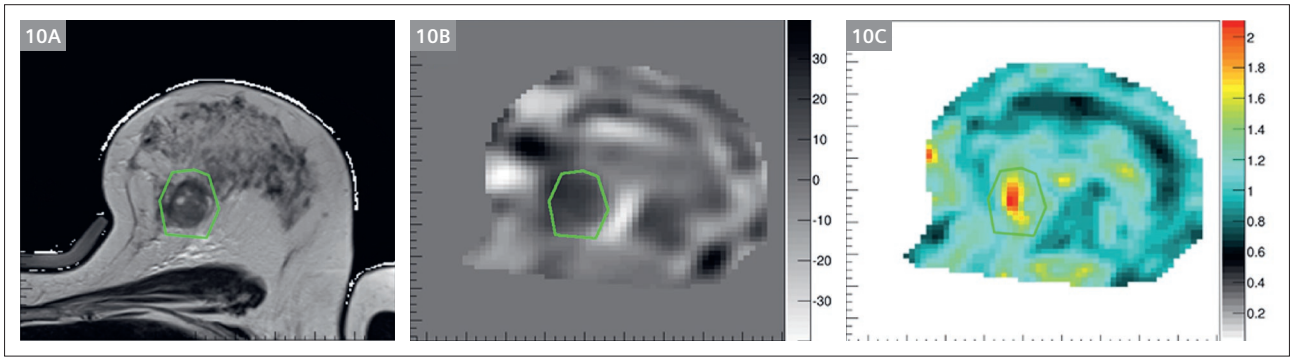

10 **3D wave-encoded MRE results in the breast**
(10A) T1-weighted anatomical image of the breast depicting a tumor within the green ROI. **(10B)** Corresponding Z-component of the curl field demonstrating that the wave propagation is not in a plane-wave fashion due to the very complex boundary conditions. **(10C)** Resulting shear wave speed image showing the tumor as a stiff object within the otherwise rather soft breast tissue. Data from King's College London, UK.

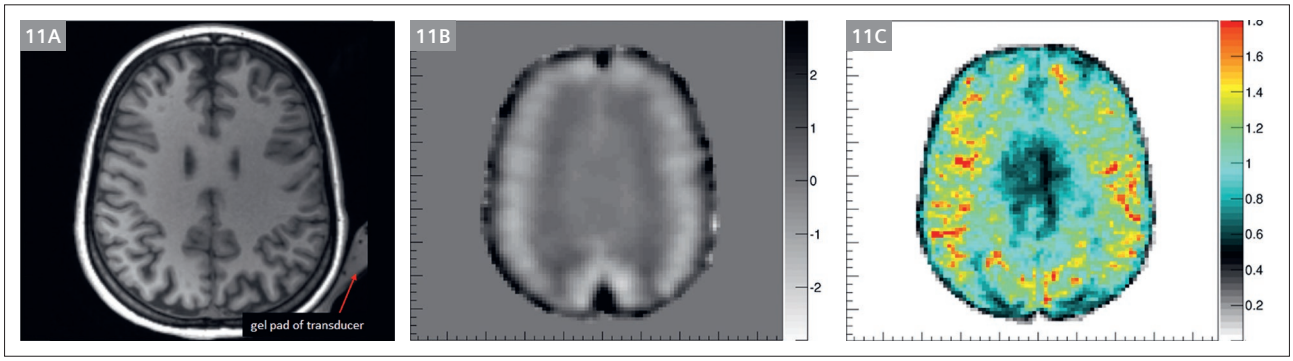

11 **3D wave-encoded MRE results in the brain**
(11A) Axial reformation of a T1-weighted 3D MPRAGE structural image of the brain. **(11B)** Corresponding image of the Z-component of the curl field showing the complex and intricate shear wave pattern within the brain. **(11C)** The resulting image of the shear wave speed shows a very high level of symmetry within the brain parenchyma and low values within the lateral ventricles, as expected [m/s]. Data from Heidelberg University Hospital, Germany.

directions (Fig. 11A). The corresponding Z-component of the curl field shows that the shear waves are propagating in a rather complex manner through the brain (Fig. 11B). The resulting shear wave speed image (Fig. 11C) depicts a high level of symmetry, as expected, from a healthy volunteer's brain. The subcortical white matter exhibits higher values of shear wave speed than cortical grey matter. Shear wave speed drops within the ventricles since cerebrospinal fluid cannot be sheared and hence exhibits very low values. The non-invasive evaluation of cerebral biomechanics is of high interest and has the potential to improve diagnosis and monitoring of various brain diseases. An obvious application is neuro-oncology as information on stiffness could not only guide the surgical approach, but also help to characterize the tumor in more depth [8]. To this end, initial clinical studies demonstrated an association between glioma stiffness and genetic features that are prognostically relevant [44, 45]. Further areas of interest include neurodegeneration, dementias, and neuroinflammation [46, 47].

Conclusions

The gravitational transducer concept, combined with advanced and fast MRI sequences and robust inversion algorithms, enables non-invasive, high-quality, and versatile assessment of biomechanics, leading to better diagnosis and staging of several clinical conditions, in particular liver fibrosis and inflammation in MASLD.

References

1 Ophir J, Céspedes I, Ponnekanti H, Yazdi Y, Li X. Elastography: a quantitative method for imaging the elasticity of biological tissues. Ultrason Imaging. 1991;13(2):111–134.
2 Lewa GJ. Elastic properties imaging by periodical displacement NMR measurements (EPMRI). Proceedings of the Ultrasonics Symposium IEEE, 1994;2:691–694.
3 Muthupillai R, Lomas DJ, Rossman PJ, Greenleaf JF, Manduca A, Ehman RL. Magnetic resonance elastography by direct visualization of propagating acoustic strain waves. Science. 1995;269(5232):1854–1857.
4 Sinkus R, Lorenzen J, Schrader D, Lorenzen M, Dargatz M, Holz D. High-resolution tensor MR elastography for breast tumour detection. Phys Med Biol. 2000;45(6):1649–1664.
5 Allen AM, Shah VH, Therneau TM, Venkatesh SK, Mounajjed T, Larson JJ, et al. The Role of Three-Dimensional Magnetic Resonance Elastography in the Diagnosis of Nonalcoholic Steatohepatitis in Obese Patients Undergoing Bariatric Surgery. Hepatology. 2020;71(2):510–521.
6 Sinkus R, Lambert S, Abd-Elmoniem KZ, Morse C, Heller T, Guenthner C, et al. Rheological determinants for simultaneous staging of hepatic fibrosis and inflammation in patients with chronic liver disease. NMR Biomed. 2018;31(10):e3956.
7 McKnight AL, Kugel JL, Rossman PJ, Manduca A, Hartmann LC, Ehman RL. MR elastography of breast cancer: preliminary results. AJR Am J Roentgenol. 2002;178(6):1411–1417.
8 Bunevicius A, Schregel K, Sinkus R, Golby A, Patz S. REVIEW: MR elastography of brain tumors. Neuroimage Clin. 2020;25:102109.
9 Fløgstad Svensson S, Fuster-Garcia E, Latysheva A, Fraser-Green J, Nordhøy W, Isam Darwish O, et al. Decreased tissue stiffness in glioblastoma by MR elastography is associated with increased cerebral blood flow. Eur J Radiol. 2022;147:110136.
10 Glaser KJ, Manduca A, Ehman RL. Review of MR elastography applications and recent developments. J Magn Reson Imaging. 2012;36(4):757–774.
11 Rump J, Klatt D, Braun J, Warmuth C, Sack I. Fractional encoding of harmonic motions in MR elastography. Magn Reson Med. 2007 Feb;57(2):388–395.
12 Guenthner C, Sethi S, Troelstra M, Dokumaci AS, Sinkus R, Kozerke S. Ristretto MRE: A generalized multi-shot GRE-MRE sequence. NMR Biomed. 2019 May;32(5):e4049.
13 Muthupillai R, Rossman PJ, Lomas DJ, Greenleaf JF, Riederer SJ, Ehman RL. Magnetic resonance imaging of transverse acoustic strain waves. Magn Reson Med. 1996 Aug;36(2):266–274.
14 Bercoff J, Tanter M, Fink M. Supersonic shear imaging: a new technique for soft tissue elasticity mapping. IEEE Trans Ultrason Ferroelectr Freq Control. 2004;51(4):396–409.
15 Kruse SA, Smith JA, Lawrence AJ, Dresner MA, Manduca A, Greenleaf JF, et al. Tissue characterization using magnetic resonance elastography: preliminary results. Phys Med Biol. 2000;45(6):1579–1590.
16 Van Houten EE, Paulsen KD, Miga MI, Kennedy FE, Weaver JB. An overlapping subzone technique for MR-based elastic property reconstruction. Magn Reson Med. 1999 Oct;42(4):779–786.
17 Sinkus R, Siegmann K, Xydeas T, Tanter M, Claussen C, Fink M. MR elastography of breast lesions: understanding the solid/liquid duality can improve the specificity of contrast-enhanced MR mammography. Magn Reson Med. 2007;58(6):1135–1144.
18 Manduca A, Lake DS, Kruse SA, Ehman RL. Spatio-temporal directional filtering for improved inversion of MR elastography images. Med Image Anal. 2003;7(4):465–473.
19 Uffmann K, Ladd M. Actuation systems for MR elastography: design and applications. IEEE Eng Med Biol Mag. 2008;27(3):28–34.
20 Van Houten EE, Doyley MM, Kennedy FE, Weaver JB, Paulsen KD. Initial in vivo experience with steady-state subzone-based MR elastography of the human breast. J Magn Reson Imaging. 2003;17(1):72–85.
21 Yin M, Talwalkar JA, Glaser KJ, Manduca A, Grimm RC, Rossman PJ, et al. Assessment of hepatic fibrosis with magnetic resonance elastography. Clin Gastroenterol Hepatol. 2007;5(10):1207–1213.e2.
22 Dittmann F, Tzschätzsch H, Hirsch S, Barnhill E, Braun J, Sack I, et al. Tomoelastography of the abdomen: Tissue mechanical properties of the liver, spleen, kidney, and pancreas from single MR elastography scans at different hydration states. Magn Reson Med. 2017;78(3):976–983.
23 Runge JH, Hoelzl SH, Sudakova J, Dokumaci AS, Nelissen JL, Guenthner C, et al. A novel magnetic resonance elastography transducer concept based on a rotational eccentric mass: preliminary experiences with the gravitational transducer. Phys Med Biol. 2019;64(4):045007.

24 Fovargue D, Kozerke S, Sinkus R, Nordsletten D. Robust MR elastography stiffness quantification using a localized divergence free finite element reconstruction. Med Image Anal. 2018;44:126–142.
25 Wochner P, Schneider T, Stockmann J, Lee J, Sinkus R. Diffusion phase-imaging in anisotropic media using non-linear gradients for diffusion encoding. PLoS One. 2023;18(3):e0281332.
26 Venkatesh SK, Yin M, Ehman RL. Magnetic resonance elastography of liver: technique, analysis, and clinical applications. J Magn Reson Imaging. 2013;37(3):544–555.
27 Guenthner C, Runge JH, Sinkus R, Kozerke S. Hadamard encoding for magnetic resonance elastography. In: Proceedings of the 25th Annual Meeting ISMRM. 2017. Honolulu.
28 Garteiser P, Sahebjavaher RS, Ter Beek LC, Salcudean S, Vilgrain V, Van Beers BE, et al. Rapid acquisition of multifrequency, multislice and multidirectional MR elastography data with a fractionally encoded gradient echo sequence. NMR Biomed. 2013;26(10):1326–1335.
29 Barth M, Breuer F, Koopmans PJ, Norris DG, Poser BA. Simultaneous multislice (SMS) imaging techniques. Magn Reson Med. 2016;75(1):63–81.
30 Darwish OI, Gharib AM, Jeljeli S, Metwalli NS, Feeley J, Rotman Y, et al. Single Breath-Hold 3-Dimensional Magnetic Resonance Elastography Depicts Liver Fibrosis and Inflammation in Obese Patients. Invest Radiol. 2023;58(6):413–419.
31 Johnson CL, McGarry MD, Van Houten EE, Weaver JB, Paulsen KD, Sutton BP, et al. Magnetic resonance elastography of the brain using multishot spiral readouts with self-navigated motion correction. Magn Reson Med. 2013;70(2):404–412.
32 Einstein A, Podolsky B, Rosen N. Can Quantum-Mechanical Description of Physical Reality Be Considered Complete? Phys Rev. 1935;47(10):777–780.
33 Landau LD, Lifshitz EM. Course of Theoretical Physics: Theory of Elasticity. 2nd English ed. Oxford: Pergamon Press; 1970. p. 165.
34 Bhatia H, Norgard G, Pascucci V, Bremer P T. The Helmholtz-Hodge Decomposition – A Survey. IEEE Transactions on Visualization and Computer Graphics. 2013;19(8):1386–1404.
35 Van Houten EE, Miga MI, Weaver JB, Kennedy FE, Paulsen KD. Three-dimensional subzone-based reconstruction algorithm for MR elastography. Magn Reson Med. 2001;45(5):827–837.
36 Verdier C. Rheological Properties of Living Materials. From Cells to Tissues. Journal of Theoretical Medicine. 2003;5(2):67–91.
37 Schiessel H, Blumen A. Mesoscopic Pictures of the Sol-Gel Transition: Ladder Models and Fractal Networks. Macromolecules. 1995;28(11):4013–4019.
38 Holm S. Waves with Power-Law Attenuation. New York: Springer, 2019.
39 Lambert SA, Näsholm SP, Nordsletten D, Michler C, Juge L, Serfaty JM, et al. Bridging Three Orders of Magnitude: Multiple Scattered Waves Sense Fractal Microscopic Structures via Dispersion. Phys Rev Lett. 2015;115(9):094301.
40 Gidener T, Ahmed OT, Larson JJ, Mara KC, Therneau TM, Venkatesh SK, et al. Liver Stiffness by Magnetic Resonance Elastography Predicts Future Cirrhosis, Decompensation, and Death in NAFLD. Clin Gastroenterol Hepatol. 2021;19(9):1915–1924.e6.
41 Sheka AC, Adeyi O, Thompson J, Hameed B, Crawford PA, Ikramuddin S. Nonalcoholic Steatohepatitis: A Review. JAMA. 2020;323(12):1175–1183.
42 Rada P, González-Rodríguez Á, García-Monzón C, Valverde ÁM. Understanding lipotoxicity in NAFLD pathogenesis: is CD36 a key driver? Cell Death Dis. 2020;11(9):802.
43 Loomba R, Adams LA. The 20% Rule of NASH Progression: The Natural History of Advanced Fibrosis and Cirrhosis Caused by NASH. Hepatology. 2019;70(6):1885–1888.
44 Pepin KM, McGee KP, Arani A, Lake DS, Glaser KJ, Manduca A, et al. MR Elastography Analysis of Glioma Stiffness and IDH1-Mutation Status. AJNR Am J Neuroradiol. 2018;39(1):31–36.
45 Svensson SF, Halldórsson S, Latysheva A, Fuster-Garcia E, Hjørnevik T, Fraser-Green J, et al. MR elastography identifies regions of extracellular matrix reorganization associated with shorter survival in glioblastoma patients. Neurooncol Adv. 2023;5(1):vdad021.
46 Hiscox LV, Schwarb H, McGarry MDJ, Johnson CL. Aging brain mechanics: Progress and promise of magnetic resonance elastography. Neuroimage. 2021;232:117889.
47 Wuerfel J, Paul F, Beierbach B, Hamhaber U, Klatt D, Papazoglou S, et al. MR-elastography reveals degradation of tissue integrity in multiple sclerosis. Neuroimage. 2010;49(3):2520–2525.
48 Bohte AE, Nelissen JL, Runge JH, Holub O, Lambert SA, de Graaf L, et al. Breast magnetic resonance elastography: a review of clinical work and future perspectives. NMR Biomed. 2018;31(10):e3932.
49 Jurrius P, Darwish O, Shifa B, Bell J, Spence J, Fovargue D, et al. Measuring the tumour IFP using MRE: a mechanical biomarker for the prediction of metastatic potential in women with invasive breast cancer. Abstract #1436 in: Proceedings of the 30th Annual Meeting ISMRM. 2021.
50 Jurrius P, Darwish O, Fovargue D, Shifa B, Welsh K, Bell J, et al. Magnetic Resonance Elastography for Early Assessment of Response to Neoadjuvant Chemotherapy in Women with Breast Cancer. Abstract #1591 in: Proceedings of the 31st Annual Meeting ISMRM. 2022.

Contact

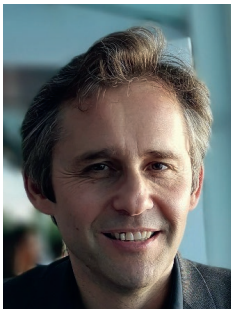

Ralph Sinkus, Ph.D.
Professor of Biomedical Engineering
at King's College London, UK,
and Research Director CNRS
at INSERM, Paris, France
King's College London
School of Biomedical Engineering &
Imaging Sciences
Rayne Institute, 4th Floor, Lambeth Wing
St. Thomas' Hospital
Westminster Bridge Road
London SE1 7EH, United Kingdom
ralph.sinkus@kcl.ac.uk

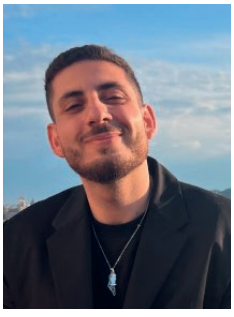

Omar Darwish
Siemens Healthineers
SHS DI MR RCT CLS BODY
Allee am Roethelheimpark 2
91052 Erlangen
Germany
omar.darwish@siemens-healthineers.com